Princeton Plasma Physics Laboratory

PPPL- 5082

PPPL-5082

Verification of Gyrokinetic Microstability Codes with an LHD Configuration

D.R. Mikkelsen, M. Nunami, T.-H. Watanabe,
H. Sugama, and K. Tanaka

November 2014

Prepared for the U.S. Department of Energy under Contract DE-AC02-09CH11466.

Princeton Plasma Physics Laboratory
Report Disclaimers

Full Legal Disclaimer

Trademark Disclaimer

PPPL Report Availability

Princeton Plasma Physics Laboratory:

http://www.pppl.gov/techreports.cfm

Office of Scientific and Technical Information (OSTI):

http://www.osti.gov/scitech/

Related Links:

U.S. Department of Energy

Office of Scientific and Technical Information

Verification of gyrokinetic microstability codes with an LHD configuration

D.R. Mikkelsen,[1, a)] M. Nunami,[2] T.-H. Watanabe,[3] H. Sugama,[2] and K. Tanaka[2]

[1)] *Princeton Plasma Physics Laboratory, P.O. Box 451, Princeton, NJ 08543*

[2)] *National Institute for Fusion Science, 322-6 Oroshi-cho, Toki-shi, Gifu 509-5292, Japan*

[3)] *Department of Physics, Nagoya University Furo-cho, Chikusa-ku, Nagoya 464-8602, Japan*

(Dated: Draft on 14 November 2014)

We extend previous benchmarks of the GS2 and GKV-X codes to verify their algorithms for solving the gyrokinetic Vlasov-Poisson equations for plasma microturbulence. Code benchmarks are the most complete way of verifying the correctness of implementations for the solution of mathematical models for complex physical processes such as those studied here. The linear stability calculations reported here are based on the plasma conditions of an ion-ITB plasma in the LHD configuration. The plasma parameters and the magnetic geometry differ from previous benchmarks involving these codes. We find excellent agreement between the independently written pre-processors that calculate the geometrical coefficients used in the gyrokinetic equations. Grid convergence tests are used to establish the resolution and domain size needed to obtain converged linear stability results. The agreement of the frequencies, growth rates and eigenfunctions in the benchmarks reported here provides additional verification that the algorithms used by the GS2 and GKV-X codes are correctly finding the linear eigenvalues and eigenfunctions of the gyrokinetic Vlasov-Poisson equations.

PACS numbers: 52.65.Tt, 52.55.Hc, 52.35.Qz

[a)] Electronic mail: dmikkelsen@pppl.gov

I. INTRODUCTION

Code benchmarks are the most complete way of verifying the correctness of implementations for the numerical solution of mathematical models for complex physical processes such as the gyrokinetic Vlasov-Poisson equations for plasma microturbulence. Many gyrokinetic codes have been benchmarked with tokamak configurations, and four such codes have been benchmarked using the quasi-axisymmetric NCSX stellarator configuration. The character of gyrokinetic solutions varies dramatically among the different families of stellarator and heliotron configurations[1], however. The dominance of the large scale toroidal variation of $|B|$ in NCSX sets it apart from other 3-D configurations with much stronger local $|B|$ wells, so the benchmarks based on the Large Helical Device (LHD)[2] (involving GKV and GENE) and W7-X[3] (involving GENE and GS2) are important milestones based on more complex geometries. Here we test the independently developed algorithms in the GKV-X and GS2 codes by comparing the geometrical coefficients and the linear stability of ion temperature gradient modes (with adiabatic electrons) using measured plasma conditions in the LHD configuration.

The GKV code[4,5] (the predecessor of GKV-X) solves the gyrokinetic Vlasov-Poisson equations, and was developed specifically for stellarator configurations, as described by analytic magnetic equlibria. It has been benchmarked linearly and nonlinearly[2] with the GENE code[6–8].

The gyrokinetic Vlasov code GKV-X[9] used here solves the gyrokinetic equation for the perturbed ion gyro-center distribution function, assuming an adiabatic electron response in a local flux-tube domain along the magnetic field line under the low β electrostatic limit. As shown in Ref. 9, GKV-X incorporates a large number of Fourier components of the magnetic field as well as full geometry of the magnetic flux-surface provided by the three-dimensional MHD equilibrium code VMEC[10]. Therefore, GKV-X can treat the equilibrium field configuration corresponding to experimental profiles of three-dimensional field of the Large Helical Device (LHD) plasmas. In Ref. 4 systematic convergence studies using the GKV code[4] were discussed and the agreement between GKV and GKV-X was confirmed[9]. The GKV-X code has also been benchmarked with both the GS2 and GENE codes in linear stability calculations for the NCSX configuration[3].

GS2 is a gyrokinetic Vlasov code[11,12] with local flux-tube geometry[13] developed originally

for strongly shaped tokamak configurations based on either analytic 'local' equilibria[14] or numerical equilibria. The axisymmetric version of GS2 has been benchmarked extensively against GENE[15–17], GYRO[15,16,18–20], and GEM[21–23]. The geometrical capabilities were extended to three-dimensional non-axisymmetric devices and benchmarked[3,24] for an NCSX equilibrium against the FULL code[25], the GENE code, and GKV-X.

The quasi-axisymmetric nature of the NCSX configuration minimizes the role of local ripple wells, so benchmarks based on it are not a strong test of stellarator-specific features of gyrokinetic stability. Here we report on the first GS2 benchmark that is based on the LHD heliotron configuration, a 'classical' type of stellarator that has much stronger local magnetic wells than NCSX. This benchmark is the first to be based on the configuration and plasma parameters of an ion-ITB plasma in LHD, which has unusually high ion temperatures and gradients that destabilize ion temperature gradient (ITG) modes[26]. Nonlinear turbulence simulations indicate that ITG turbulence produces the level of 'anomalous' heat flux needed to augment the neoclassical flux and balance the ion heating[27], so validation of the gyrokinetic model for turbulent transport is also planned with more complete simulations.

The calculations reported here are based on an LHD ion-ITB discharge already described in Refs. 26, 28, and 29. This type of plasma has large ion temperatures and gradients, providing ideal conditions for validating models of ITG turbulence. For computational convenience we adopt several simplifications for this verification study: there is a single ion species, the density and temperature of ions and electrons are taken to be equal, and the electron response is purely adiabatic.

The independently calculated geometrical coefficients used in the benchmarks are compared in Section II. In Section III we describe the details of the gyrokinetic stability calculations, and summarize the resolution convergence tests. The growth rates, real frequencies, and eigenfunctions are compared in Section IV, and the results are summarized in Section V.

II. COMPARISON OF GEOMETRICAL COEFFICIENTS

The geometrical coefficients for both GS2 and GKV-X are derived from the same 3D magnetic equilibrium calculated by the VMEC code[10]. The equilibrium is based on the experimental conditions of the ion-ITB, or high-T_i, phase of LHD discharge 88343, as de-

scribed in Ref. 26, which also compares these coefficients in the low- and high-T_i phases. The field line that is the basis for the flux-tube geometry used here is in the magnetic surface at r/a=0.50, and we've chosen the one with the label $\alpha_\mathrm{o} = \pi/10$ and the 'ballooning angle' $\theta_\mathrm{o} = 0$ because this maximizes the growth rate. In more physical terms, the ballooning angle coincides with the center of the theta domain, $\theta = 0$, which is located on the outer midplane of LHD at a toroidal location where the plasma cross section is elongated horizontally and is up-down symmetric.

The calculation of these coefficients for GKV-X is described in detail in Ref. 9, which also contains a benchmark with the model analytic equilibrium used by GKV.

The geometrical coefficients used by GS2 are ultimately calculated by VVBAL[30], which is embedded in the GIST[31] pre-processing package for GS2 and GENE that is used to prepare geometrical input files for 3D configurations. The use of VVBAL for gyrokinetic work was first described in Ref. 25, while the GIST formulation is described in Ref. 31 where it is benchmarked with an independently developed field line tracing method[32]. Definitions of the dimensionless geometrical coefficients used by GS2 are provided in Ref. 33, which also has comprehensive documentation of GS2's geometrical conventions, the gyrokinetic equation, and normalizing conventions for dimensionless variables.

The normalizing length and magnetic field strength used by GIST are defined in Eqs. (75-76) of Ref. 31, and differ from those for axisymmetric configurations as described in Ref. 33. Specifically, lengths are normalized by the average minor radius, a, that is calculated by VMEC from the volume enclosed by the last closed flux surface. Magnetic fields are normalized by B_a, which is derived from the toroidal flux enclosed by the last closed flux surface: $B_\mathrm{a} = 2\phi_\mathrm{edge}/a^2$.

The variation along the magnetic field line of two codes' calculation of the GS2 definition of normalized magnetic field strength is compared in Fig. 1. This coefficient, named `bmag`, is simply $|B|/B_\mathrm{a}$.

The theta dependence of the perpendicular wavenumber is complex, and three coefficients are used in GS2, see Eqs. (3.67-3.70) in Ref. 33. These are denoted (g_1, g_2, g_3) or (`gds2`, `gds21`, `gds22`), we use the latter notation here since it is based on variable names in GS2. These are compared in Figures 2-4, where the appropriate combinations of metric coefficients derived for GKV-X are used to calculate the comparison quantities; see Eq. (26) of Ref. 9 for the GKV-X formulation of the perpendicular wavenumber. In this and other figures the GS2

dimensionless coefficient is compared with a combination of GKV-X geometrical coefficients that reproduces the GS2 definition and is normalized according to GS2 conventions.

The oscillatory terms in GS2's curvature- and ∇B-drift coefficients are quite similar to each other, and the secular terms are identical; see Eqs. (3.61-3.65) in Ref. 33. In GKV-X there is no difference in the oscillatory coefficients since the small pressure gradient contribution is ignored in order to maintain consistency with the low β limit of the gyrokinetic equations. The related coefficients for GKV-X are components of Eq. (24) of Ref. 9, and these terms are used to construct the quantities compared with GS2 coefficients. Once again the agreement is excellent, as shown in Figures 5-6.

The very close match between the geometrical coefficients shown here builds confidence that the independently formulated and implemented geometrical calculations are correct. This agreement also implies that any significant difference in the linear stability results will be caused by the gyrokinetic solution algorithms, not the tiny differences in the geometrical coefficients.

III. GRID RESOLUTION, CONVERGENCE, AND MODE IDENTIFICATION

The two gyrokinetic Vlasov codes used in this work, GKV-X and GS2, were developed quite independently, as were the algorithms for deriving geometric terms from a 3D magnetic equilibrium. The codes use different pairs of velocity-space coordinates, as described below. The typical grid spacing schemes for the coordinate aligned with the magnetic field differ, as does the extent of the domain.

The gyrokinetic Vlasov code GKV-X used here solves the gyrokinetic equation (in the low β electrostatic limit) for the ion's perturbed gyrocenter distribution function (assuming the electron response is adiabatic) in a local flux-tube domain oriented along the magnetic field line. As shown in Ref. 9, GKV-X incorporates a large number of Fourier components of the magnetic field as well as full geometry of the magnetic flux-surface obtained from the three-dimensional MHD equilibrium code VMEC[10]. Therefore, GKV-X can treat the equilibrium field configuration corresponding to experimental profiles of the three-dimensional field of the Large Helical Device (LHD) plasmas. The calculations shown in the next section employed 1024 grid points, on the domain $-\pi < \theta < \pi$, of the coordinate aligned with the field line,

and 128 and 64 grid points, respectively, on the $v_\parallel$ and μ grids, where μ is the magnetic moment (additional detail is provided in Ref. 9).

As discussed in the case of GS2 below, grid resolution convergence of the coordinate aligned with the magnetic field line was examined for the mode with peak growth rate, $k_{\rm y}\rho_{\rm i}$= 0.5. When the number of grid points aligned with the field line is reduced to 512 and 256, the growth rates are changed by 1.0% and 1.4%, respectively. Therefore, it is confirmed that robust results are guaranteed with 1024 grid points along the coordinate aligned with the field line.

The other code used here is GS2, a Vlasov (or continuum) gyrokinetic code with a comprehensive range of capabilities thought to be important for turbulence in the core of toroidal plasmas, including multiple species, fully kinetic descriptions of all species, collisions, fully electromagnetic fluctuations, and sheared flows[11,12], but these features are not included in the electrostatic simulations with adiabatic electrons reported here. The geometrical capabilities and previous benchmarks have been discussed in the Introduction and the previous section. For computational convenience we adopt several simplifications for this verification study: a single ion species, the density and temperature of ions and electrons are taken to be equal, and the electron response is purely adiabatic. Linear stability properties of the fastest growing eigenmode are calculated independently (and simultaneously, in parallel operation) for each specified perpendicular wavenumber with a time-implicit initial-value finite-difference algorithm in the ballooning (or "flux-tube") limit.

The perpendicular wavenumber used in GS2 is dimensionless, normalized by the inverse gyro-radius of the majority ion (hydrogen here). The GS2 definition of thermal velocity and gyro-radius are unconventional so we have adopted the GKV-X normalization for $k_{\rm y}\rho_{\rm i}$ and for growth rates and real frequencies (which are normalized by the rate $v_{\rm th,i}/R_{\rm o}$), where $v_{\rm th,i} = \sqrt{T_{\rm i}/m_{\rm i}}$. The values of the wavenumber spectrum ($k_{\rm y}\rho_{\rm i}$=0.1,0.2,...,0.8) are chosen to extend well below and above the wavenumber with the peak growth rate. Grid resolution convergence studies were carried out for the entire wavenumber spectrum, but the sensitivity of the mode with peak growth rate, $k_{\rm y}\rho_{\rm i}$=0.5, is specified in the discussion.

For the calculations reported here the GS2 grid for θ, the coordinate aligned with the magnetic field line, is fully correlated with the λ grid, the coordinate that is related to the velocity space pitch angle for trapped particles (see section 3.4 of Ref. 3). Every θ grid point is located at a trapped particle bounce point corresponding to one of the λ grid locations.

Similarly for every λ grid point, all of its bounce locations (that is, in every local well that is accessible for that λ) are in the θ grid. This follows the philosophy of the grid generator developed for the original axisymmetric version of GS2, as described in detail in section 5.2 of Ref. 33.

The λ grid points are equally spaced between endpoints that correspond to the most deeply trapped orbit in the deepest $|B|$ well, and the largest barely trapped orbit that has bounce locations at both ends of the θ domain. Apart from the deepest $|B|$ well in the domain, there is usually no θ grid point at a local minimum of $|B|$ and the θ step size becomes relatively large near every minimum and maximum of $|B|$ (see Fig. 7). The step size could be made small near all extrema of $|B|$, but the computational cost would be quite serious: a large number of λ grid points *and* a very large number of θ grid points, leading to very large memory requirements and long computation times even for linear calculations.

Alternate grid-building algorithms have been explored but the scheme sketched above is reliable when it does not lead to numerical instability, which has unmistakably unphysical eigenfunction structure and unusually large growth rates. In these cases the instability may be cured by slightly modifying the grid: additional θ grid points can be inserted into the regions with large θ step sizes, but no corresponding λ grid points are added. The absence of a corresponding λ grid point produces a small truncation error in velocity space integrals because extremely deeply trapped orbits are not represented. Alternatively (or in combination with the grid modification) an upwind differencing scheme may cure the numerical instability, but this first-order scheme can introduce a noticeable inaccuracy when used with a grid that contains large θ steps. Tests with a variety of grid types and grid spacings show that the upwind differencing scheme has a small effect on the results when there are no large θ steps. GKV-X is normally run with an upwind differencing scheme, but with its typical small θ grid spacing this does not affect the results significantly. It is therefore quite appropriate to compare the GS2 results without upwind differencing to the GKV-X results since both choices are accurate.

For the calculations shown in the next section 46 trapped pitch angles were used, and the 2451 θ grid points have an average spacing of 0.008. The global maximum θ step size is 0.05, and the typical maximum step size near an extremum of $|B|$ is 0.03. When the number of trapped pitch angles was raised to 65, the number of θ grid points rose to 3477, the global maximum and typical local maximum step size were 0.045 and 0.025, and the growth rate

changed by up to 3% at the ends of the $k_y\rho_i$ spectrum, but less than 1% near the peak growth rates. The robustness of the results are further demonstrated by simulations with the number of λ and θ grid points reduced to 20 and 1027, respectively. The peak growth rate is reduced by less than 1%, while the largest change, for $k_y\rho_i$=0.2, is only -3%

Gaussian integration is used for integrals over the energy grid, so these converge with relatively sparse grids. For the results shown in the next section we used 16 energies; with 24 energies the growth rates change by up to a bit less than 1%, and with only 8 the growth rates change by 4% or less. Gaussian integration is also used for the integrals over the pitch angle of the passing particles. The standard Gaussian order is 10, and reducing this to 5 changes the growth rates by less than 1%.

The dimensionless time step (using GKV-X normalization), $\Delta t(v_{\mathrm{th,i}}/R_{\mathrm{o}})$, is 0.22 for the results shown in the next section. When it is reduced to 0.09 the growth rates change by 0.5% at the lowest $k_y\rho_i$, but much less for other wavenumbers.

As shown in the next section, the growth rates calculated by GKV-X and GS2 differ significantly for high $k_y\rho_i$, and those differences far exceed the size of the inaccuracies due to finite grid resolution discussed in this section.

IV. LINEAR STABILITY

We now compare the growth rates, real frequencies, and eigenfunctions from GKV-X and GS2. The calculations reported here are based on the experimental conditions of the ion-ITB, or high-T_i phase of LHD discharge 88343, as described in Ref. 26. The grid resolutions are described in the previous section, as are the convergence tests which demonstrate that the results reported here represent very well converged results from both GS2 and GKV-X, so the differences are ascribed to the differing solution algorithms, not to inaccuracy caused by coarse grid resolution.

The field line that is the basis for the flux-tube geometry employed here is in the magnetic surface at r/a=0.50; we've chosen $\alpha_{\mathrm{o}} = \pi/10$ and the 'ballooning angle' $\theta_{\mathrm{o}} = 0$ because this maximizes the growth rate. In more physical terms, the ballooning angle coincides with the center of the theta domain, $\theta = 0$, which is located on the outer midplane of LHD at a toroidal location where the plasma cross section is elongated horizontally and is up-down symmetric. The values of the wavenumber spectrum ($k_y\rho_i$=0.1,0.2,...,0.8, using the GKV-X

normalization convention) are chosen to extend well below and above the wavenumber with the peak growth rate.

As shown in Figs. 8-9 the eigenfunction shape has a 'ballooning' character that is typical of ITG modes, and the width encompasses many local ripple wells. The θ domain for GS2 extends to ± 9.5 radians, considerably beyond the point where the eigenfunctions have become very small.

For all $k_{\mathrm{y}}\rho_{\mathrm{i}}$ studied here the overall eigenmode structure is the same for both codes, and much of the minor structure is also very closely matched. There are, however, significant local differences that are largest near major local extrema of both the real and imaginary parts. As shown in the part b) of Figs. 8-9 these differences are extended over an entire 'period' of the $|B|$ local ripple so they appear to have nothing to do with GS2's large θ grid steps very near *every* local extremum of $|B|$. This is confirmed by calculations not shown here that use grids with no large θ step sizes, but do reproduce the local departures from GKV-X seen in Figs. 8-9. Similarly, upwind differencing does not play a role in these local differences.

The frequency and growth rate spectra for both codes are compared in Fig. 10 for two values of the temperature gradient parameter. The growth rates agree very well at low $k_{\mathrm{y}}\rho_{\mathrm{i}}$ but the difference is $\sim$7% at the peak growth rate and grows as $k_{\mathrm{y}}\rho_{\mathrm{i}}$ increases. For a/L_{Ti}=4 the difference does not exceed 10% in the range considered, which is similar to previous linear benchmarks that have reported differences as large as $\sim$7%. Closer to threshold however, with a/L_{Ti}=2, the relative size of the difference at the highest $k_{\mathrm{y}}\rho_{\mathrm{i}}$ (with much weaker growth rates) is amplified by the larger cancellation between the driving and damping terms. Similar $k_{\mathrm{y}}\rho_{\mathrm{i}}$ dependence of the difference has also been reported in two instances[3,17], but this is not evident in most gyrokinetic benchmarks.

V. SUMMARY

Code benchmarks are an important method of verifying the correctness of implementations for the solution of models for complex physical processes such as the gyrokinetic Vlasov-Poisson equations for plasma microturbulence. We have extended the benchmarks of the GKV-X and GS2 codes by comparing the geometrical coefficients and the linear stability of ion temperature gradient modes (with adiabatic electrons) using measured plasma

conditions of an ion-ITB plasma in LHD. We found excellent agreement between the independently written pre-processors that calculate the geometrical coefficients used in the gyrokinetic equations. The less good, but acceptable, agreement in the linear stability benchmarks reported here provides additional verification that the independently developed algorithms used by the GS2 and GKV-X codes are correctly calculating the linear eigenvalues and eigenfunctions of the gyrokinetic equations.

We thank J.A. Baumgaertel, G.W. Hammett and P. Xanthopoulos for helpful discussions. This work has been done under the collaboration research of the National Institute for Fusion Science. It is a pleasure to acknowledge cooperation and discussions with Professors K. Komori, O. Kaneko and H. Yamada of the National Institute for Fusion Science. One of the authors (M.N.) is supported in part by the Japanese Ministry of Education, Culture, Sports, Science and Technology, Grant (No. 22760660 and 26820398), and by Japan / U. S. Cooperation in Fusion Research and Development. This work was supported by U.S. Department of Energy Contract No. DE-AC02-76CH03073. Use of parallel computer clusters at PPPL is gratefully acknowledged.

REFERENCES

[1]G. Rewoldt, L.-P. Ku, and W. M. Tang, Phys. Plasmas **12**, 102512 (2005).

[2]P. Xanthopoulos, A. Mischchenko, P. Helander, H. Sugama, and T.-H. Watanabe, Phys. Rev. Lett. **107**, 245002 (2011).

[3]J. A. Baumgaertel, *Simulating the Effects of Stellarator Geometry on Gyrokinetic Drift-Wave Turbulence*, Ph.D. thesis, Princeton University (2012), `http://www.princeton.edu/plasma/academics/graduate-theses/thesis-files/2012/JBaumgaertel_PhDthesis.pdf`.

[4]T.-H. Watanabe and H. Sugama, Nucl. Fusion **46**, 24 (2006).

[5]T.-H. Watanabe, H. Sugama, and S. Ferrando-Margalet, Nucl. Fusion **47**, 1383 (2007).

[6]F. Jenko, W. Dorland, M. Kotschenreuther, and B. N. Rogers, Phys. Plasmas **7**, 1904 (2000).

[7]T. Görler, X. Lapillonne, S. Brunner, T. Dannert, F. Jenko, F. Merz, and D. Told, J. Comp. Phys. **230**, 7053 (2011).

[8]P. Xanthopoulos, F. Merz, T. Görler, and F. Jenko, Phys. Rev. Lett. **99**, 035002 (2007).

[9]M. Nunami, T.-H. Watanabe, and H. Sugama, Plasma Fusion Res. **5**, 016 (2010).

[10]S. P. Hirshman and O. Betancourt, J. Comp. Phys. **96**, 99 (1991).

[11]M. Kotschenreuther, G. Rewoldt, and W. M. Tang, Comp. Phys. Comm. **88**, 128 (1995).

[12]W. Dorland, F. Jenko, M. Kotschenreuther, and B. N. Rogers, Phys. Rev. Lett. **85**, 5579 (2000).

[13]M. A. Beer, S. C. Cowley, and G. W. Hammett, Phys. Plasmas **2**, 2687 (1995).

[14]R. L. Miller, M. S. Chu, J. M. Greene, Y. R. Lin-Liu, and R. E. Waltz, Phys. Plasmas **5**, 973 (1998).

[15]W. M. Nevins, J. Candy, S. Cowley, T. Dannert, A. Dimits, W. Dorland, C. Estrada-Mila, G. W. Hammett, F. Jenko, M. J. Pueschel, and D. E. Shumaker, Phys. Plasmas **13**, 122306 (2006).

[16]A. M. Dimits, W. M. Nevins, D. E. Shumaker, G. W. Hammett, T. Dannert, F. Jenko, M. J. Pueschel, W. Dorland, S. Cowley, J. N. Leboeuf, T. L. Rhodes, J. Candy, and C. Estrada-Mila, Nucl. Fusion **47**, 817 (2007).

[17]P. Xanthopoulos, D. Mikkelsen, F. Jenko, W. Dorland, and O. Kalentev, Phys. Plasmas **15**, 122108 (2008).

[18]J. Candy and R. E. Waltz, J. Comp. Phys. **186**, 545 (2003).

[19]J. Candy, R. Waltz, and W. Dorland, Phys. Plasmas **11**, L25 (2004).

[20]R. V. Bravenec, C. Holland, J. Candy, and M. Barnes, Phys. Plasmas **18**, 122505 (2011).

[21]W. M. Nevins, S. E. parker, Y. Chen, J. Candy, A. Dimits, W. Dorland, G. W. Hammett, and F. Jenko, Phys. Plasmas **14**, 084501 (2007).

[22]Y. Chen, S. Parker, W. Wan, and R. Bravenec, Phys. Plasmas **20**, 092511 (2013).

[23]R. Bravenec, Y. Chen, J. Candy, W. Wan, and S. Parker, Phys. Plasmas **20**, 104506 (2013).

[24]J. A. Baumgaertel, E. A. Belli, W. Dorland, W. Guttenfelder, G. W. Hammett, D. R. Mikkelsen, G. Rewoldt, W. M. Tang, and P. Xanthopoulos, Phys. Plasmas **18**, 122301 (2011).

[25]G. Rewoldt, L.-P. Ku, W. M. Tang, and W. A. Cooper, Phys. Plasmas **6**, 4705 (1999).

[26]M. Nunami, T.-H. Watanabe, H. Sugama, and K. Tanaka, Plasma Fusion Res. **6**, 1403001 (2011).

[27]M. Nunami, T.-H. Watanabe, H. Sugama, and K. Tanaka, Phys. Plasmas **19**, 042504 (2012).

[28]K. Ida, M. Yoshinuma, M. Osakabe, K. Nagaoka, M. Yokoyama, H. Funaba, C. Suzuki, T. Ido, A. Shimizu, I. Murakami, N. Tamura, H. Kasahara, Y. Takeiri, K. Ikeda, K. Tsumori, O. Kaneko, S. Morita, M. Goto, K. Tanaka, K. Narihara, T. Minami, I. Yamada, and the LHD Experimental Group, Phys. Plasmas **16**, 056111 (2009).

[29]K. Tanaka, C. Michael, L. Vyacheslavov, H. Funaba, M. Yokoyama, K. Ida, M. Yoshinuma, K. Nagaoka, S. Murakami, A. Wakasa, T. Ido, A. Shimizu, M. Nishiura, Y. Takeiri, O. Kaneko, K. Tsumori, K. Ikeda, M. Osakabe, K. Kawahata, and LHD Experiment Group, Plasma Fusion Res. **5**, S2053 (2010).

[30]W. A. Cooper, Plasma Phys. & Controlled Fusion **34**, 1011 (1992).

[31]P. Xanthopoulos, W. A. Cooper, F. Jenko, Y. Turkin, A. Runov, and J. Geiger, Phys. Plasmas **16**, 082303 (2009).

[32]P. Xanthopoulos and F. Jenko, Phys. Plasmas **13**, 092301 (2006).

[33]E. Highcock, *The Zero-Turbulence Manifold in Fusion Plasmas*, Ph.D. thesis, Merton College, University of Oxford (2012), `http://arxiv.org/abs/1207.4419`.

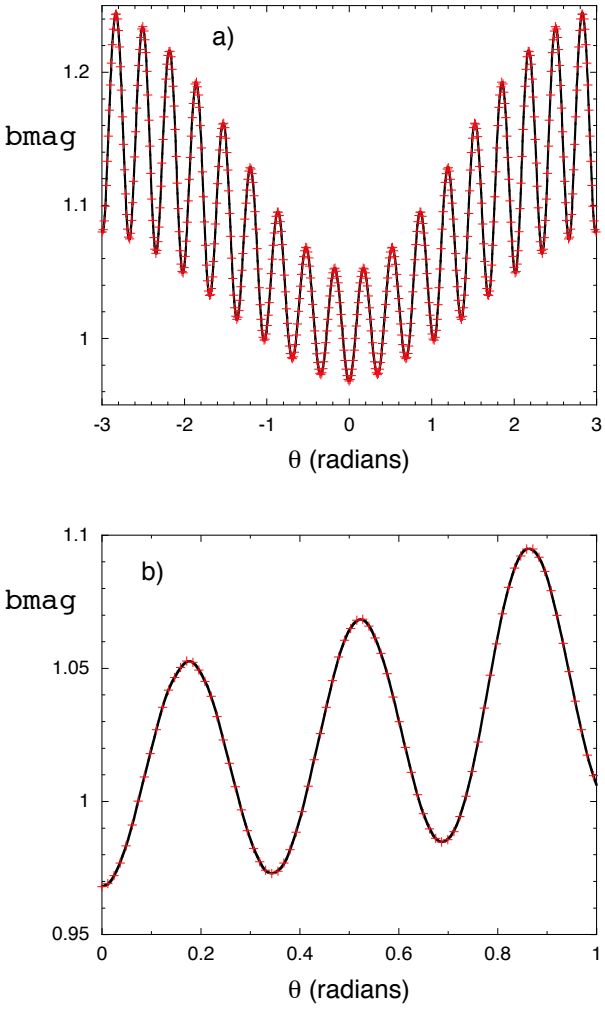

FIG. 1. a) Normalized magnetic field strength `bmag`$= |B|/B_{\rm a}$, for GS2, the solid line, and GKV-X, the plus signs (red online). The outboard midplane is located at $\theta = 0$, the inboard midplane is at approximately $\theta = \pm\pi$. b) Zoom of local ripple wells near $\theta = 0$.

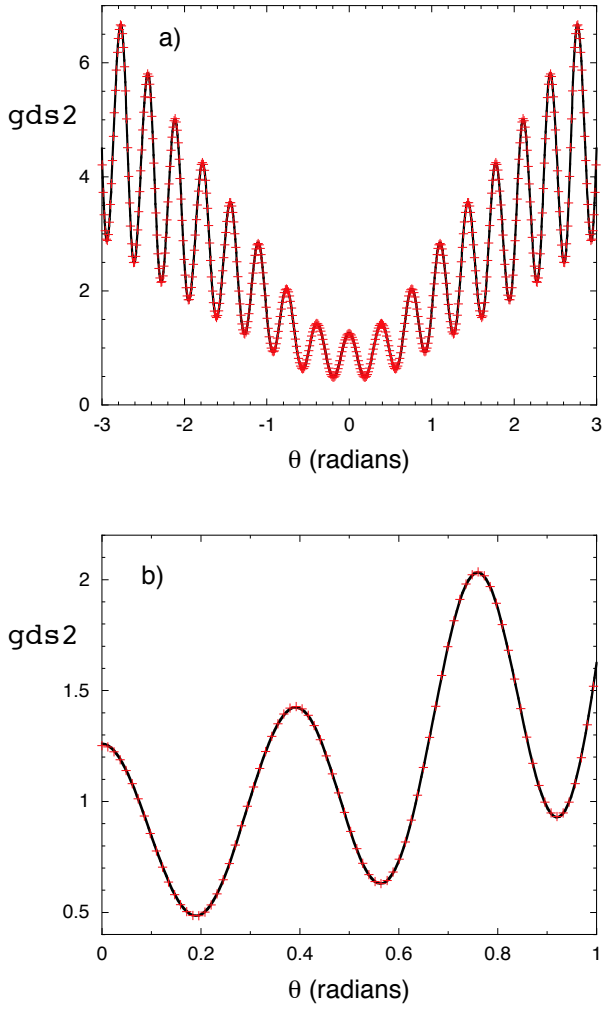

FIG. 2. a) The dimensionless `gds2` coefficient for GS2, the solid line, and GKV-X, the plus signs (red online). b) Zoom of local ripple wells near $\theta = 0$.

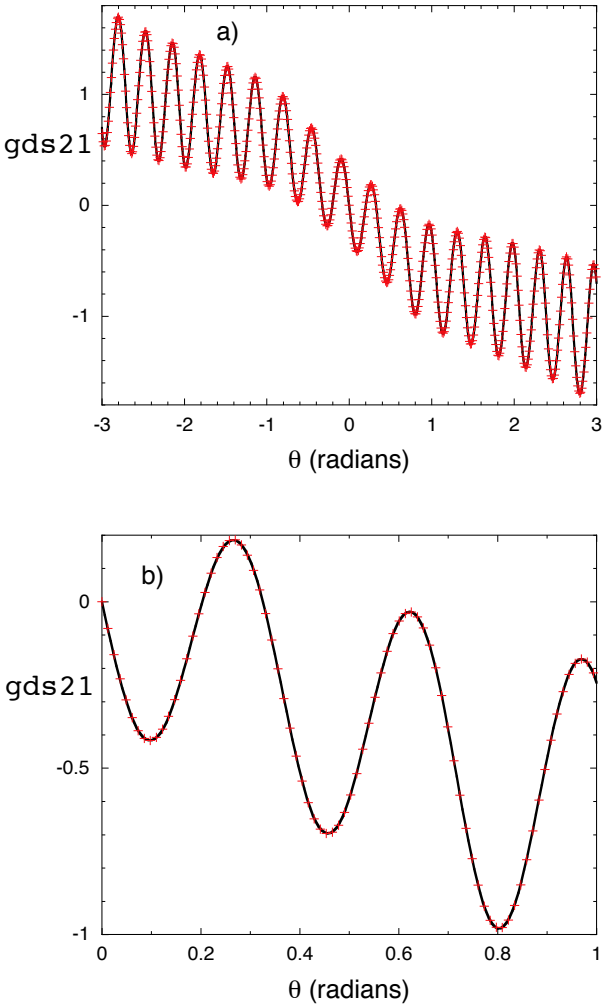

FIG. 3. a) The dimensionless `gds21` coefficient for GS2, the solid line, and GKV-X, the plus signs (red online). b) Zoom of local ripple wells near $\theta = 0$.

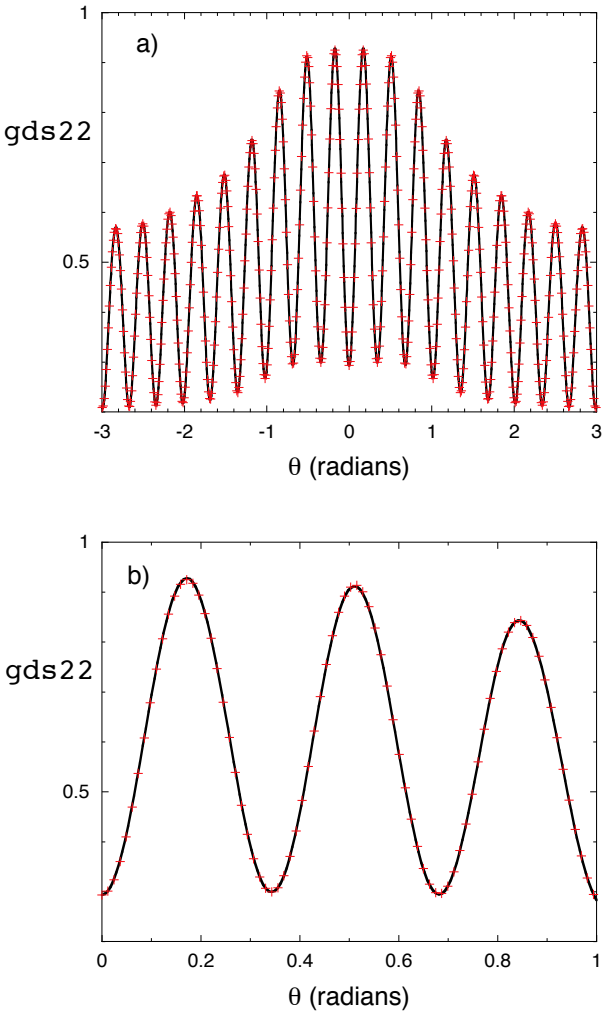

FIG. 4. a) The dimensionless `gds22` coefficient for GS2, the solid line, and GKV-X, the plus signs (red online). b) Zoom of local ripple wells near $\theta = 0$.

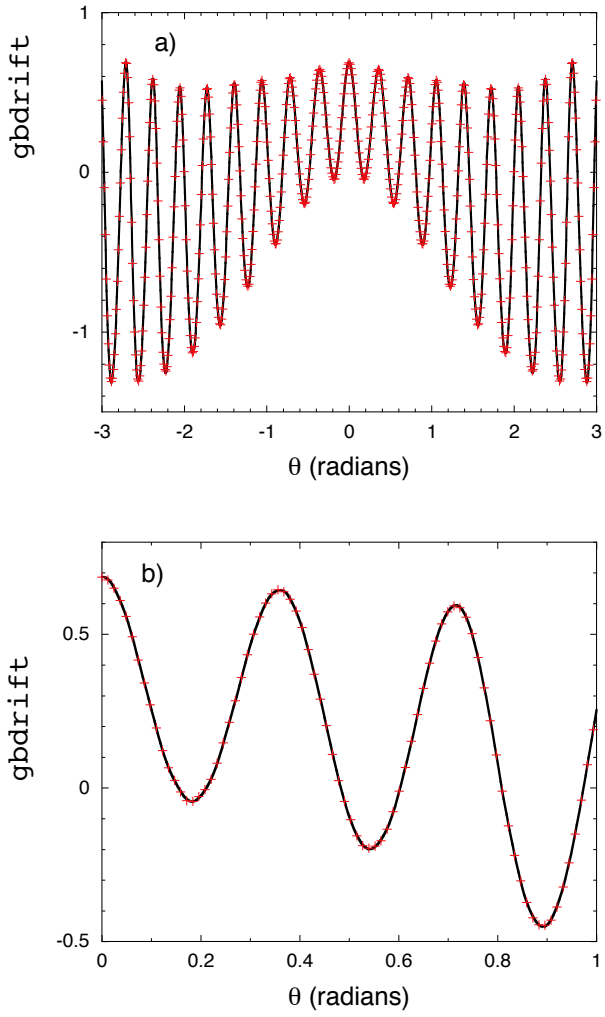

FIG. 5. a) The dimensionless `gbdrift` coefficient for GS2, the solid line, and GKV-X, the plus signs (red online). b) Zoom of local ripple wells near $\theta = 0$.

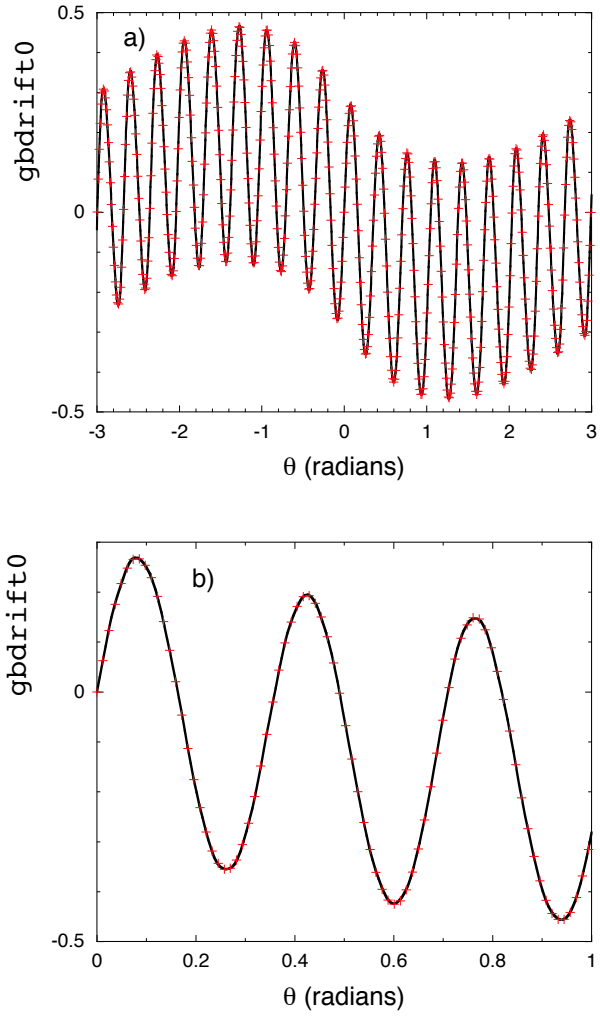

FIG. 6. a) The dimensionless `gbdrift0` coefficient for GS2, the solid line, and GKV-X, the plus signs (red online). b) Zoom of local ripple wells near $\theta = 0$.

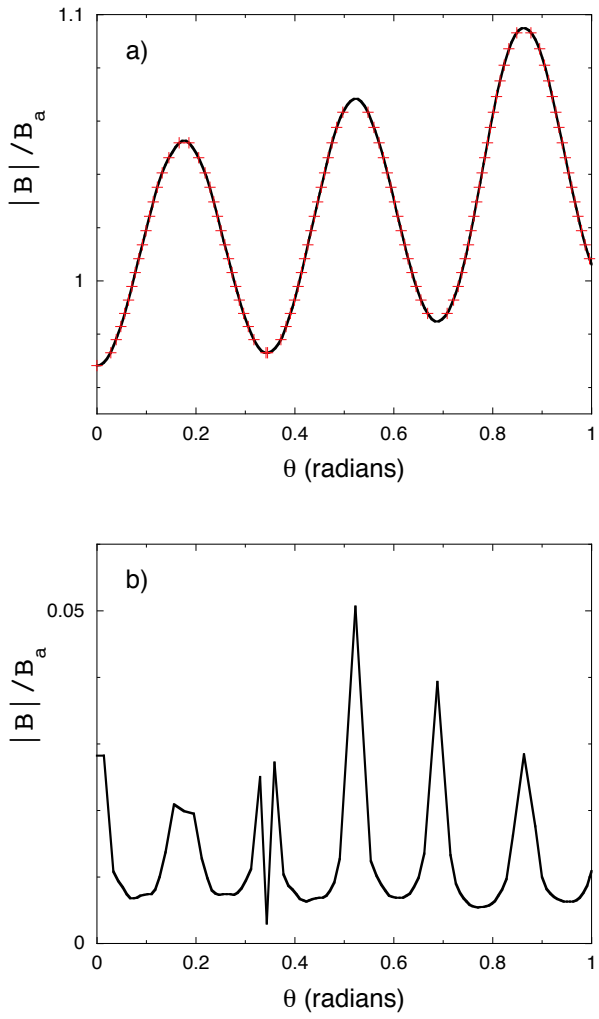

FIG. 7. a) Plus signs (red online) denote $|B|/B_{\rm a}$ at the GS2 θ grid locations; the solid line has higher resolution to fill the regions with large step size. Part b) shows the step size for the θ grid; note the large θ steps at all local extrema of $|B|$.

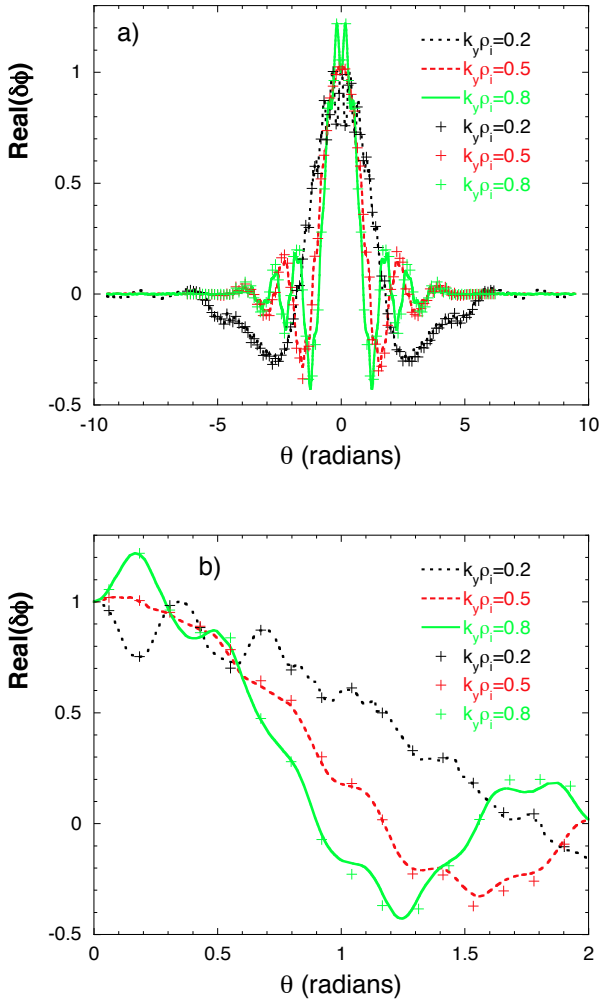

FIG. 8. a) The real part of the fluctuating potential for GS2, as lines, and GKV-X, as plus signs (color online); wavenumber is indicated by line type, $k_{\rm y}\rho_{\rm i}$=0.2: widely spaced dashes, $k_{\rm y}\rho_{\rm i}$=0.5: closely spaced dashes, $k_{\rm y}\rho_{\rm i}$=0.8: solid line. b) Zoom of $0 < \theta < 2$.

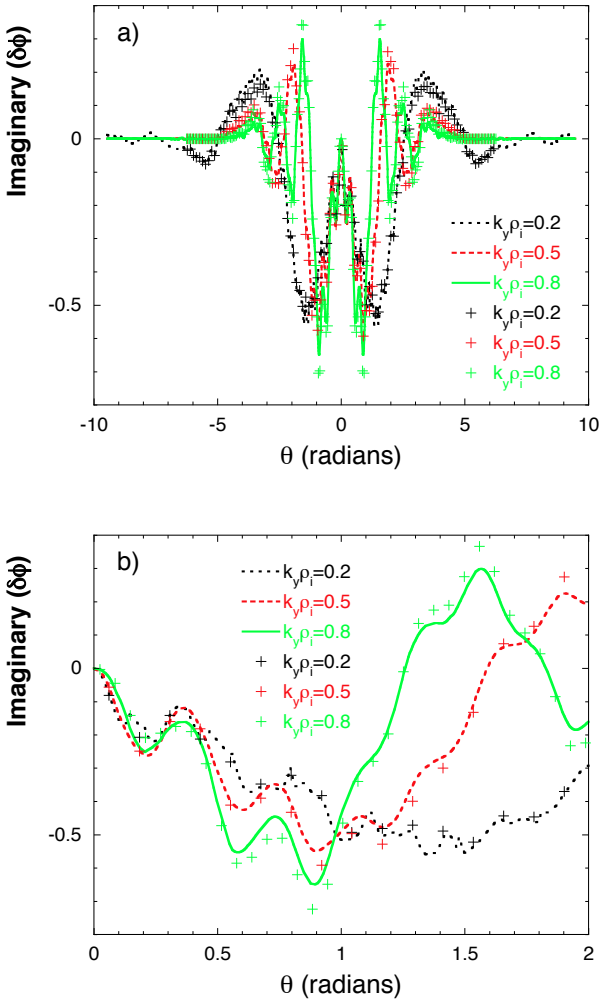

FIG. 9. a) The imaginary part of the fluctuating potential for GS2, as lines, and GKV-X, as plus signs (color online); wavenumber is indicated by line type, $k_{\rm y}\rho_{\rm i}$=0.2: widely spaced dashes, $k_{\rm y}\rho_{\rm i}$=0.5: closely spaced dashes, $k_{\rm y}\rho_{\rm i}$=0.8: solid line. b) Zoom of $0 < \theta < 2$.

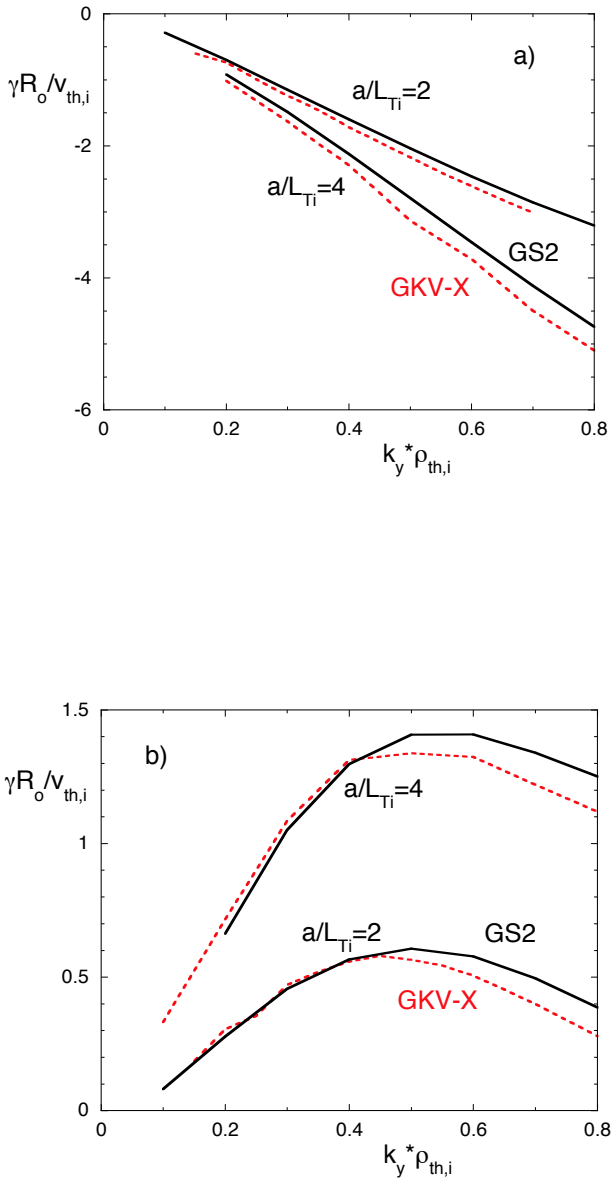

FIG. 10. a) The dimensionless frequency for GS2 (solid line) and GKV-X (dashed line, red online), and b) the dimensionless growth rate, for two values of the temperature gradient parameter.

Princeton Plasma Physics Laboratory
Office of Reports and Publications

Managed by
Princeton University

under contract with the
U.S. Department of Energy
(DE-AC02-09CH11466)

P.O. Box 451, Princeton, NJ 08543
Phone: 609-243-2245
Fax: 609-243-2751

E-mail: publications@pppl.gov
Website: http://www.pppl.gov